Article

Research of Seismogenic Structures of the 2016 and 2022 Menyuan Earthquakes, in the Northeastern Tibetan Plateau

Junyi Wang [1,2], **Lin Ding** [1,2,*], **Jiankun He** [1,2], **Fulong Cai** [1,2], **Chao Wang** [1,2] and **Zongkun Zhang** [1,2]

1   State Key Laboratory of Tibetan Plateau Earth System, Resources and Environment (TPESRE), Institute of Tibetan Plateau Research, Chinese Academy of Sciences, Beijing 100101, China
2   University of Chinese Academy of Sciences, Beijing 100049, China
*   Correspondence: dinglin@itpcas.ac.cn

Abstract: On 8 January 2022, a Moment Magnitude (Mw) 6.7 earthquake occurred in Menyuan, China. The epicenter was located in the western segment of the Lenglongling fault of the Qilian-Haiyuan fault zone. In this area, the Mw 5.9 Menyuan earthquake on 26 August 1986 and the Mw 5.9 Menyuan earthquake on 21 January 2016 successively occurred. The seismogenic structures of the 1986 and 2016 earthquakes are on the Northern Lenglongling fault, which is a few kilometers away from the Lenglongling fault. After the 2022 Menyuan earthquake, we collected GF-7 and Sentinel-1 satellite images to measure the surface deformation of the earthquake sequence. Based on the elastic dislocation theory, the fault model and fault slip distribution of the 2016 and 2022 Mengyuan earthquakes were inverted using coseismic surface displacements. The results show that the 2016 event is a reverse event, with the maximum coseismic surface displacement on LOS reaching 8 cm. The strike, dip, and rake of the earthquake rupture were $139°$, $41°$, and $78°$, with the maximum slip reaching 0.6 m at a depth of 8 km. The surface rupture of the 2022 Mw 6.7 earthquake ran in the WNW–ESE direction with a maximum displacement on LOS of 72 cm. The main seismogenic fault of the 2022 event was the western segment of the Lenglongling fault. The strike, dip, and rake of the rupture were $112°$, $85°$, and $3°$, with the maximum slip reaching 4 m at a depth of 4 km. The Coulomb failure stress change shows that the earthquake sequence generated a considerable positive Coulomb failure stress of more than 2 bar. These observations suggest that the earthquake sequence around Menyuan is mainly governed by the activities of the Lenglongling fault around the northeastern Tibetan Plateau. In addition, their sequential occurrences could be related to earthquake-triggering mechanisms due to stress interaction on different deforming faults. Thus, the Lenglongling fault has received a great amount of attention regarding its potential earthquake hazards.

Keywords: Menyuan earthquake; Lenglongling fault; InSAR; Coulomb stress; the northeastern Tibetan Plateau

1. Introduction

In the past 35 years, three Mw ~6 earthquakes have occurred around Menyuan County, Qinghai Province. Tectonically, these earthquakes were all distributed in the Qilian mountains (Figure 1), a strong active deformation belt in the northeastern Tibetan Plateau that has experienced several devastating Mw 7–8 earthquakes in its history [1–6]. On 8 January 2022, a Mw 6.7 earthquake occurred at a depth of ~ 10 km [1]. Focal mechanism solutions showed that this event was dominated by strike-slip faulting (Table in Section 4.2). Field observations indicated that the seismogenic fault of this earthquake could be the western Lenglongling fault, together with a simultaneous rupture of the secondary Tuolaishan fault [1]. Previous to this, the Mw 5.9 Menyuan earthquake on 21 January 2016 occurred ~40 km southeast of the 2022 event [2], and the Mw 5.9 Menyuan earthquake on 26 August 1986 occurred ~20km southeast of the 2022 event [3]. Previous studies have suggested that the 1986 Mw 5.9 earthquake demonstrated normal fault activity dominated by dip-slip

components [3], but some studies have suggested that the 1986 event was a reverse-fault earthquake [4]. The seismogenic structures of the 1986 and the 2016 Menyuan earthquakes are on the Northern Lenglongling fault [2,5]. The Northern Lenglongling fault is an associated fault to the northwest of the Lenglongling fault, which is correspondingly bent by the tectonic thrust of the left-lateral shear at the end of the Lenglongling fault [5]. The Lenglongling fault is located on the northeastern Tibetan Plateau and has been mainly characterized by left-lateral strike-slip movement with local dip-slip components since the Holocene [6,7]. The activities of the seismogenic fault in these three events are very different, showing the relatively complex tectonic setting of the Lenglongling fault zone, and there are apparent differences in the stress distribution in different areas of the fault zone [8,9]. Although the Lenglongling fault has released three moderate earthquakes, the area has not experienced earthquakes with magnitudes greater than seven.

Qilianshan is one of the most significant active rupture areas on the Tibetan Plateau, with frequent seismic activities. The 1986, 2016, and 2022 events provide an opportunity to study the fault system on the northeastern Tibetan Plateau by analyzing the seismic deformation characteristics and regional Coulomb stress changes, which are essential for studying the region's seismicity and predicting future seismic hazard zones. The Synthetic Aperture Radar Interference (InSAR) technique has achieved remarkable results in studying coseismic deformation and the inversion of seismic source parameters due to its significant advantages, such as all-day time and comprehensive coverage [10–14].

In this study, we researched three Mw ~6 earthquakes in the area based on InSAR and discuss the latest seismic activity in the northeastern Tibetan Plateau by analyzing the coseismic deformation fields, geometric parameters of fault inversions, and Coulomb stresses of the earthquakes. Section 2 analyzes the regional tectonic background. Section 3 analyzes the surface deformation of the 2016 event and the 2022 event. The distribution characteristics of the coseismic surface rupture zone are determined based on GF-7 satellite images of the 2022 Menyuan earthquake. Sentinel-1 SAR images generate the coseismic deformation fields of the 2016 and 2022 earthquakes. Section 4 inverts the seismic fault model and calculates the Coulomb stress. The elastic half-space rectangular dislocation theory is utilized to invert the fault model and fault slip distribution [15]. The seismogenic structures of the earthquakes and the regional seismogenic structures are discussed in Section 5. Finally, Section 6 summarizes the results of this paper.
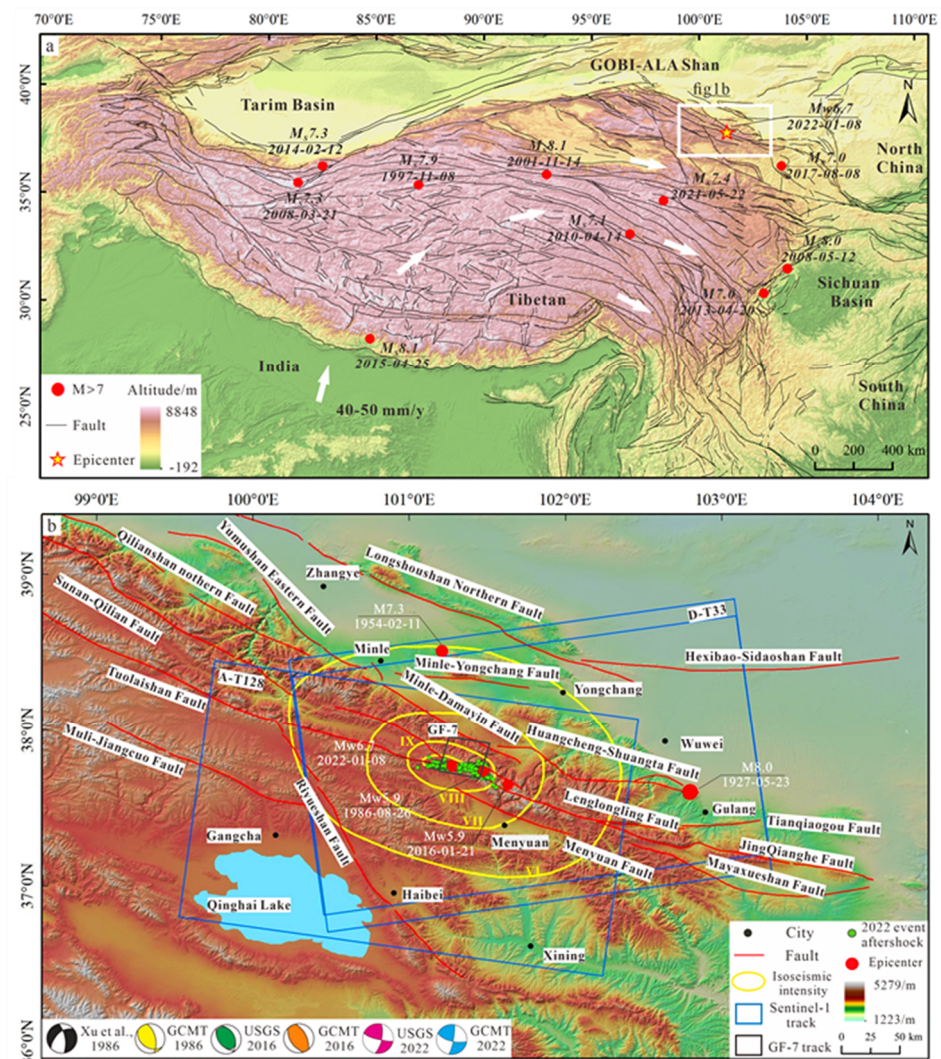
2. Tectonic Setting

Since the collision of the Indian plate with the Eurasian plate at 65 Ma, the continuous movement of the Indian plate in the north-north-east (NNE) direction has caused the rapid uplift of the Tibetan Plateau and expansion into the interior of the continent [16–18]. The deformation of the northern Tibetan Plateau is mainly controlled by the east-north-east (ENE)-direction left-lateral strike-slip fault zones (such as the Altun fault zone, the Haiyuan fault zone, and the East Kunlun fault zone), the west-north-west (WNW)-direction reverse fault zones (such as the Northern Qilianshan reverse fault zone, the Northern Qaidam reverse fault zone, and the Qimatage reverse fault zone), and the north-north-west (NNW)-direction right-lateral strike-slip fault zones (such as the Olshan fault and the Riyueshan fault) [19,20]. The northeastern Tibetan Plateau is undergoing NE-direction shortening (Figure 1a), counterclockwise rotation, and east-south-east (ESE)-direction extrusion tectonic deformation under north-east (NE)-direction tectonic stress [21].

The Lenglongling fault is a considerable portion of the Qilian-Haiyuan fault zone [22,23], which has a NE strike and a length of ~120 km. The western segment of the fault is adjacent to the Tuolaishan fault, and the eastern segment is connected to the Tianqiaogou-Huangyangchuan fault (Figure 1b). Along the Lenglongling fault zone, there are gullies, terraces, ridges, and moraines, which are dislocated by the fault with a major left-lateral component [24]. According to the moraine in situ cosmogenic nuclide, the gullies' and terraces' dislocations combined with chronological data show a 2–19 mm/y left-lateral slip rate since the late Quaternary [6,7,25,26]. Interpretation of satellite images and field geolog-

ical investigation considered an associated reverse fault of the Lenglongling fault called the Northern Lenglongling fault, which has demonstrated a general NE strike and minor surface deformation since the late Quaternary [27]. The Tuolaishan fault is a left-lateral strike-slip fault, with a NE strike and a dip angle of 50°–65° at ~300 km [22,28,29]. According to the GPS data calculations, the slip rate of the Tuolaishan fault is 4.1 ± 0.1 mm/y [30,31].

The Qilian-Haiyuan fault zone, where the Tuolaishan and the Lenglongling faults are located, is one of the regions with the highest frequency of seismic activity in China, in a tectonic setting prone to strong earthquakes [32–34]. This area experienced the 1954 Shandan Ms 7.3 earthquake and the 1927 Gulang Ms 8.0 earthquake [35]. The Lenglongling fault is in the Tianzhu seismic gap on the Qilian-Haiyuan fault zone, which is also an essential potential seismogenic fault in the high-magnitude earthquake hazard area in the middle segment of Qilianshan [6,19].

Figure 1. Regional tectonic setting. (**a**) Study area on the northeastern Tibetan Plateau. The fault data are from [36]. The Ms ≥ 7 earthquake data are from [24]. (**b**) Location of the study area. The isoseismic intensity is from [1]. The aftershock data are from [37].

3. Satellite Image Processing

In recent years, remote sensing has been widely used in resource exploration [38], disaster investigation [39], and feature target monitoring [40] due to its significant advantages in Earth observation. InSAR, as a remote sensing technology, has provided many research results in the observation of surface deformation, such as earthquakes, volcanic

eruptions, and glacial sliding, due to its significant advantages [41–43], among which seismic observation is one of the most mature fields of application of InSAR technology.

3.1. GF-7 Satellite Image Interpretation

The GF-7 satellite is the first civil sub-meter optical transmission stereo mapping satellite in China [41]. The GF-7 satellite can provide panchromatic stereo image pairs with a resolution better than 0.7 m and multispectral images with a resolution better than 3.2 m, and can carry out civil 1:10,000 large-scale satellite stereo mapping [42]. After the 2022 Mw 6.7 Menyuan earthquake, the distribution characteristics of coseismic surface ruptures zones were determined based on the GF-7 satellite images. The satellite data processing was mainly based on ENVI software, and the correction was performed by correlating the pixel coordinates of satellite data with the ground point coordinates. The SRTM1 DEM data were selected for processing, such as orthorectification correction, to obtain panchromatic and multispectral data. By fusing the multispectral data with the panchromatic data, a fused image with 0.65 m resolution could be obtained to carry out the later analysis of surface rupture zone interpretation [43].

The 2022 Menyuan earthquake formed surface rupture zones along the faults (Figure 2). The surface rupture zone of fault F1 is distributed along the Tuolaishan fault, and it can be identified in the image with a length of ~2 km (Figure 2b). Fissures and ruptures mainly dominate this area through the piedmont proluvial fan. The surface rupture zone of fault F2 developed along the Lenglongling fault, and the identifiable length in the image is ~22 km (Figure 2c–f). The surface rupture zone of the western section of fault F2 is more continuous and has tension fissures, extrusion bulges, and other types of surface rupture. Due to the snow cover, the satellite image could not identify the obvious surface rupture zone in the eastern section. Based on the interpretation of GF-7 images, we obtained the surface rupture zone distribution and the strike of the ruptures.

3.2. Sentinel-1 SAR Images Processing

The coseismic deformation fields of the two earthquakes were obtained from Sentinel-1 SAR images covering the area of the 2016 and 2022 events (Table 1). The InSAR coseismic deformation field and phase gradient of surface deformation were obtained using GMTSAR software [44–46]. Interferometric processing used 30 m-spatial-resolution SRTM1 DEM data to eliminate the topographic phase and perform geocoding. The interferometric filtering process selected the Gaussian filter and phase unwrapping based on the Snaphu algorithm [47]. After phase unwrapping and geocoding, we used the GASOS (Generic Atmospheric Correction Online Service) atmospheric delay phase model to correct the atmospheric delay of the interferometric errors [48–50]. The software ISCE (Interferometric Synthetic Aperture Radar Scientific Computing Environment) [51] was applied to obtain the pixel offset tracking (POT) of the 2022 Menyuan earthquake.

Table 1. Sentinel-1 SAR image parameters.

| Earthquake	Path	Flight Direction	Master	Slave	Spatial Baseline/m	Time Baseline/d
2016/01/21	128	Ascending	2016/01/13	2016/02/06	27.8	24
	33	Descending	2016/01/18	2016/02/11	30.28	24
2022/01/08	128	Ascending	2022/01/05	2022/01/17	36.41	12
	33	Descending	2021/12/29	2022/01/10	40.27	12

3.2.1. Coseismic Deformation Field

As shown in Figure 3a–b, the coseismic deformation field of the ascending and descending tracks of the 2016 Menyuan earthquake was continuous. The maximum LOS (Line of Sight) displacement of the ascending track was 6 cm, and the maximum LOS displacement of the descending track was 8 cm. The surface coseismic deformation field was 20 km × 16 km. The 2022 Menyuan earthquake maximum LOS displacement of

the ascending track was 65 cm, and the maximum LOS displacement of the descending track was 72 cm. The surface deformation range of the coseismic deformation field was 35 km × 20 km, and the long axis of the deformation field ran in the WNW–ESE direction. The opposite sign of the deformation variables observed from the seismic ascending and descending track images indicated that the fault was dominated by strike-slip motion [52]. The coseismic deformation field of the 2022 Menyuan earthquake's ascending and descending tracks could determine that the 2022 event was a strike-slip earthquake.
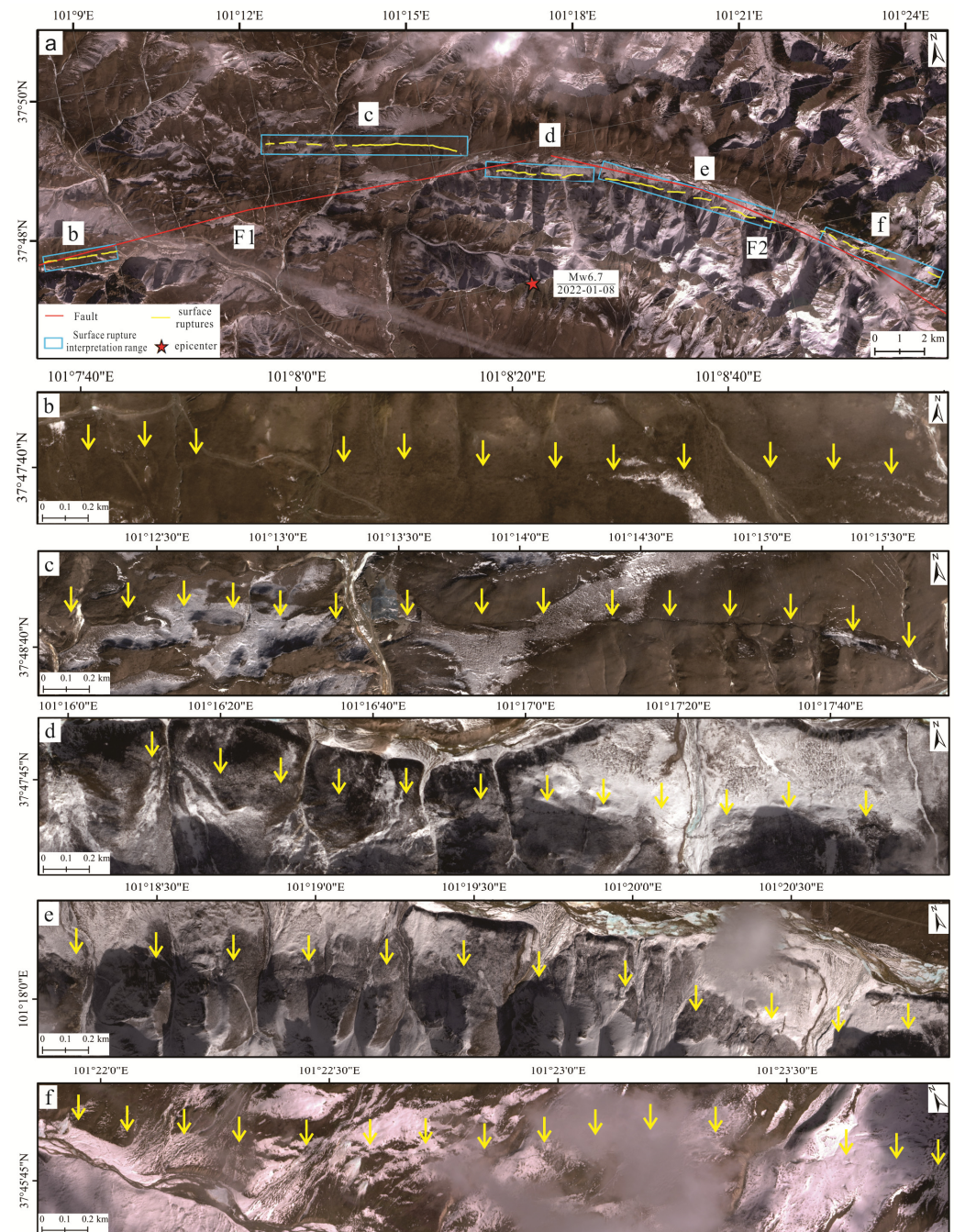
Figure 2. Surface rupture zone interpretation results of the 2022 Menyuan earthquake. F1 is the Tuolaishan fault. F2 is the Lenglongling fault.
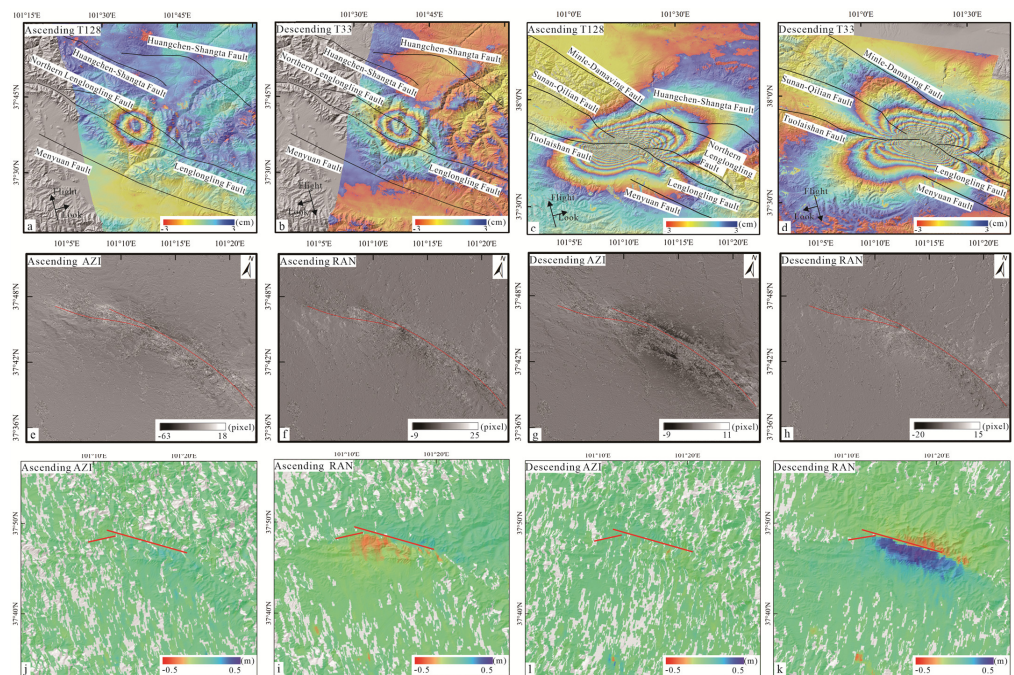
Figure 3. SAR image processing results. (**a**,**b**) InSAR coseismic deformation fields of the 2016 Menyuan earthquake's ascending and descending tracks. (**c**,**d**) InSAR coseismic deformation fields of the 2022 Menyuan earthquake's ascending and descending tracks. (**e**–**h**) Phase gradient images of the 2022 Menyuan earthquake's ascending and descending tracks. (**j**–**k**) POT images of the 2022 Menyuan earthquake's ascending and descending tracks.

3.2.2. Phase Gradient

For field geological investigations, phase gradient maps can indicate fault rupture distributions [46]. The phase gradient is directly generated from the interferogram of the real and imaginary parts [53]. Unlike standard interferograms, they can be superimposed directly without phase unwrapping [53]. The phase gradient of the 2022 Menyuan earthquake's ascending and descending tracks showed better results of the characteristics of seismic surface deformation (Figure 3e–h). Although the phase gradient can show the surface deformation features better when large, it can also extract the deformation characteristics in the azimuth and range directions of the ascending and descending tracks. In particular, the phase gradient showed that the surface deformation zone of the Lenglongling fault crosses the surface deformation zone of the Tuolaishan fault, and GF-7 images and InSAR results showed that the surface deformation zones generally followed the NWW–SEE direction.

3.2.3. Pixel Offset Tracking

Pixel offset tracking (POT) can obtain the range and azimuth deformation using SAR images, and the monitoring accuracy of POT is related to the spatial resolution of SAR images [54]. The POT results of the 2022 Menyuan earthquake's ascending and descending tracks revealed that azimuth deformation was not significant in comparison to the range deformation (Figure 3j–k). Although the measurement accuracy of the POT is lower than that of InSAR, the method can acquire azimuth deformation and is relatively less affected by phase decoherence. The results showed that the surface deformation zones of the 2022 Menyuan earthquake were divided into two sections along the Lenglongling fault and the Tuolaishan fault, while the surface deformation was mainly concentrated on the Lenglongling fault.

4. Fault Inversion and Coulomb Stress

By obtaining ground displacement observations using InSAR, fault geometry parameters can be determined in inversion based on geophysical models [55]. The nonlinear inversion algorithm can solve the location and geometric morphological parameters of the fault [56]. After determining information, such as fault location and geometric parameters, a suitable linear equation is established to perform linear inversion of the fault, which can obtain results such as fault slip distribution and seismic source parameters [57]. Based on the InSAR coseismic deformation field of the 2016 and 2022 Menyuan earthquakes, the fault model parameters of the two earthquakes were inverted using elastic half-space rectangular dislocation theory [15]. According to the results of fault inversion and the focal mechanism solution, the distributed slip model of the fault and the change in the Coulomb stress that the earthquakes caused were established.

4.1. Inversion of Fault Geometric Parameters

The 2016 and 2022 events' interferometric results were first inverted using the gCent software package. gCent (geodetic Centroid) software was used to invert and obtain geometric parameters such as strike, dip, slip angle, and maximum slip for the single-fault model of the 2016 event and the 2022 event. The software adopted a domain algorithm to carry out inversion, which enabled the fast inversion of fault model parameters [58–62]. The gCent selected the variable data downsampling method to improve the inversion rate and reduce the impact of image noise [63]. Table 2 shows the parameters for the 2016 and 2022 Menyuan earthquakes found by the final inversion. Figure 4 shows the coseismic deformation field, model-fitted deformation field, and residuals. Figure 4a–f shows the inversion results of the 2016 Menyuan earthquake, and Figure 4g–l shows those of the 2022 Menyuan earthquake. Figure 4i,l shows residuals from the 2022 Menyuan earthquake in the near-field region. The main reasons for residuals are snow and glacier cover in the region affecting the acquisition of deformation field; low coherence or even lost coherence caused by large gradient deformation in the seismic near-field region; untangling errors caused by low coherence; and the simplification of the geometry of active faults.

Table 2. Focal mechanism parameters of the 1986, 2016, and 2022 Menyuan earthquakes.

Earthquake	Parameter Source	Magnitude	Strike/°	Dip/°	Rake/°	Length/ km	Width/ km	Maximum Slip/m
1986/8/26	GCMT	Mw5.9	125	37	55	-	-	-
			346	60	113	-	-	-
	[3]	Ms6.4	50	45	-	-	-	-
2016/1/21	GCMT	Mw5.9	146	43	83	-	-	-
			335	47	96	-	-	-
	USGS	Mw5.9	141	50	79	-	-	-
			337	41	103	-	-	-
	[64]	Mw5.9	134	43	68	24	20	0.45
	[12]	Mw5.9	141	40	-	9.1	4.2	0.3 (strkie slip)/ 0.1 (dip slip)
	This study [1]	Mw5.9	142	44	73	9.4	7.7	0.61
	This study [2]	Mw5.9	139	41	78	8.3	7.2	0.57
2022/1/8	GCMT	Mw6.7	104	82	1	-	-	-
			14	89	172	-	-	-
	USGS	Mw6.6	104	88	15	-	-	-
			13	75	178	-	-	-
	[9] TLSF [3]	Mw6.6	86	85.6	38	-	-	3.8
	LLLF [4]		105	85.6	38	-	-	

Table 2. *Cont.*

Earthquake	Parameter Source		Magnitude	Strike/°	Dip/°	Rake/°	Length/ km	Width/ km	Maximum Slip/m
	[65]	TLSF [3]	Mw6.7	104	80	0	10	16	2.5
		LLLF [4]		109	80	5	20	16	3
	This study [1]		Mw6.6	108	80	5	24	14	3.5
	This study [2]	TLSF [3]	Mw6.7	89	82	6	7.6	6.3	2.7
		LLLF [4]		112	85	3	21	13	4

[1] gCent software inversion result, [2] PSOKINV software inversion result, [3] is the Tuolaishan fault (TLSF), [4] is the Lenglongling fault (LLLF).
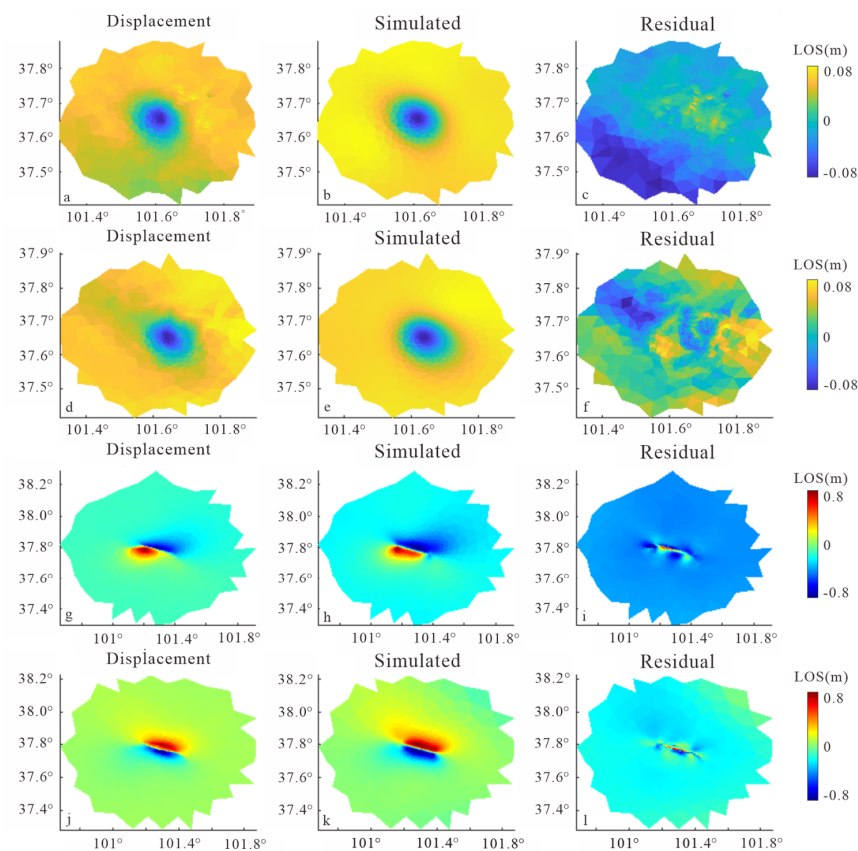
**Figure 4.** Coseismic deformation fields of the 2016 and 2022 Menyuan earthquakes.

4.2. Distributed Slip Model

The inversion of fault slip distribution was performed using the PSOKINV software package [66]. PSOKINV introduced a two-step inversion strategy [67]: the first step was based on nonlinear inversion to obtain the fault model, such as location, strike, dip, and rake of the fault, and the second step obtained the fault slip distribution model by linear inversion. PSOKINV used the Multipeaks Particle Swarm Optimization (MPSO) algorithm to achieve nonlinear parameter inversion under optimal fitting conditions [68,69]. We adopted the quadtree sampling method to process the InSAR coseismic deformation field before the inversion [70]. Using PSOKINV software in the first step of nonlinear inversion, we refer to the inversion results of the gCent software package as the initial model for the nonlinear inversion. According to the InSAR coseismic deformation field (Figure 3), the surface deformation field of the 2016 Menyuan earthquake exhibited a single-fault deformation feature and the 2022 Menyuan earthquake along the Lenglongling fault and the Tuolaishan fault formed two surface deformation zones. The fault model for the 2016

event was set as a single fault, and the 2022 Menyuan earthquake was set as a double-fault model. The 2016 Mengyuan earthquake fault length range was set at 6–10 km, and the width was set at 5–9 km. The 2022 Menyuan earthquake F1 fault length was set at 8–15 km, and the width was set at 5–9 km. The F2 fault length was set at 16–23 km, and the width was set at 6–15 km.

The second step of linear inversion was to obtain the slip on the fault surface. The spatial distribution of the faults was determined based on the fault geometry parameters obtained from nonlinear inversion of the PSOKINV, extending the length and width of the fault plane, respectively. The inversion results are shown in Table 2. The fault length and width of the 2016 Menyuan earthquake extended to 12 km × 16 km. The length and width of the 2022 event F1 fault extended to 10 km × 15 km, and the F2 fault extended to 25 km × 15 km, respectively. For the fault slip model, the seismic fault surface was discretized into 0.25 km × 0.25 km subfaults. Figure 5 shows the inversion results of the distributed slip model of the two earthquakes. The 2016 Menyuan earthquake's maximum slip was 9 km underground (Figure 5a). The maximum slip was ~ 0.6 m, and the inversion calculation moment magnitude was Mw 5.9. The 2022 Menyuan earthquake's maximum slip was located at ~ 5 km underground, the maximum slip was ~ 4 m, and the inversion calculation moment magnitude was Mw 6.7 (Figure 5b). The strike, dip, and rake of the fault obtained from inversion are consistent with those of other focal mechanisms (Table 2).
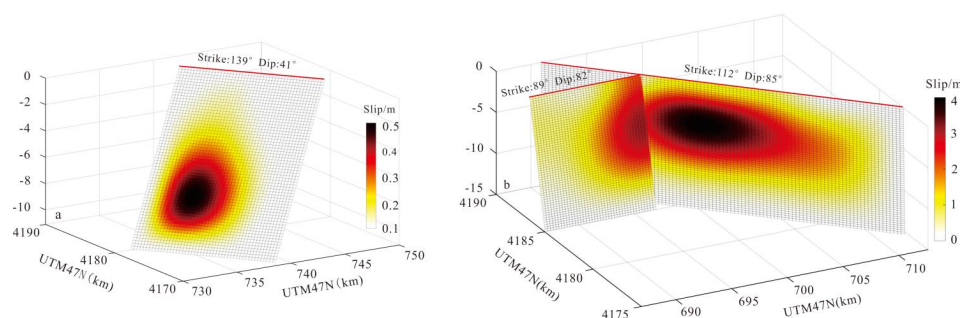

Figure 5. Distributed slip model of (**a**) the 2016 Menyuan earthquake and (**b**) the 2022 Menyuan earthquake.

4.3. Coulomb Stress Change

When an earthquake occurs, the dislocation on the seismogenic fault will change the stress distribution in the region and may trigger or delay the occurrence of earthquakes on active faults in adjacent regions [71–74]. The Coulomb stress was calculated using the Coulomb3 software package, and the friction coefficient was set to 0.4 [75–77]. The 1986 and 2016 Menyuan earthquakes both occurred on the Northern Lenglonglling fault, with the distance between the epicenters of the two earthquakes being ~20km; but previous studies suggested that the 1986 Menyuan earthquake demonstrated normal fault activity dominated by dip-slip components [3]. The debate regarding the focal mechanism of the 1986 Menyuan earthquake is related to the complex tectonic processes in the area. In addition, there was a lack of field investigations and limited measurement data at the time. Interpretations of satellite images and field geological investigation considered that the Northern Lenglonglling fault is a reverse fault of the Lenglonglling fault, which has a general NE strike [27]. The GCMT (https://www.globalcmt.org (accessed on 26 December 2022)) results showed that the focal mechanism of the 1986 Menyuan earthquake was a reverse earthquake (Table 2). The GCMT fault interface 1 results of the 1986 event showed that the strike, dip, and rake were 125°, 37°, and 55°, respectively. The fault interface 1 production and kinematic properties were more consistent with the production of the Northern Lenglonglling fault. As the geometric parameters of the source fault, we selected the GCMT source mechanism solution for the 1986 event. The empirical equation [78] was applied to calculate the length and width of the 1986 fault. Based on the PSOKINV uniform slip inversion results (Table 2) of the 2016 and 2022 events of the fault model, we calculated the Coulomb stress changes caused by the three earthquakes. According to the inversion

results, the maximum sliding depths of the 2016 event and the 2022 event inversion were 8 km and 4 km, respectively. The Coulomb stress change was calculated at depths of 5 km and 10 km, respectively.

In Figure 6a,b, the source fault is the seismogenic fault of the 1986 Menyuan earthquake, and the receiving fault is the seismogenic fault of the 2016 Menyuan earthquake. In Figure 6c,d, the source fault is the seismogenic fault of the 2016 Menyuan earthquake, and the receiving fault is the seismogenic fault of the 2022 Menyuan earthquake. It can be seen that the 2016 and 2022 Menyuan earthquakes were in a region of positive Coulomb stress change. Moreover, the stress of the Lenglongling fault zone was increased. In Figure 6e,f, the source fault is the seismogenic fault of the 2016 Menyuan earthquake, and the receiving fault is the seismogenic fault of the 2022 Menyuan earthquake. It can be seen that the 2016 Menyuan earthquake produced positive Coulomb stress on the 2022 Menyuan earthquake. The 2022 Menyuan earthquake fault was located in the same enhanced Coulomb stress region as the 1986 and 2016 Menyuan earthquakes. The Coulomb stress of the 1986 and 2016 events indicated that it affected the occurrence of the 2022 Mengyuan earthquake. Suppose the seismogenic fault of the 2022 Menyuan earthquake is the source fault, and the Lenglongling fault is the receiver fault (Figure 6g,h). In this case, it can be seen that the 2022 Menyuan earthquake influenced the regional Coulomb stress distribution. The Coulomb stress enhancement of the Northern Lenglongling fault, the Tuolaishan fault, the Lenglongling fault, the eastern Minle-Yongchang fault, and the western Dabanshan fault increased by more than 0.2 bar, and the risk of earthquake occurrence increased.
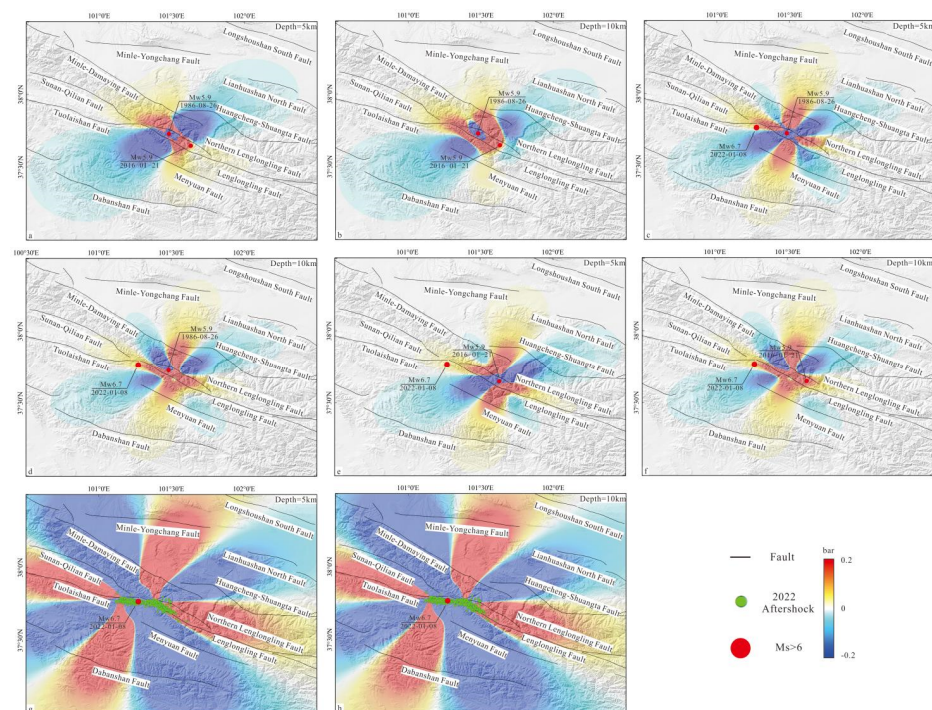

Figure 6. Coulomb stress change. (**a**,**b**) The 1986 Menyuan earthquake seismogenic fault was set as the source fault, the 2016 Menyuan earthquake seismogenic fault was set as the receiver fault, and the Coulomb stress was calculated at depths of 5 km and 10 km, respectively. (**c**,**d**) The 1986 Menyuan earthquake's seismogenic fault was set as the source fault, the 2022 Menyuan earthquake seismogenic fault was set as the receiver fault, and the Coulomb stress was calculated at depths of 5 km and 10 km, respectively. (**e**,**f**) The 2016 Menyuan earthquake seismogenic fault was set as the source fault, the 2022 Menyuan earthquake seismogenic fault was set as the receiver fault, and the Coulomb stress was calculated at depths of 5 km and 10 km, respectively. (**g**,**h**) The 2016 Menyuan earthquake seismogenic fault was set as the source fault, the 2022 Menyuan earthquake seismogenic fault was set as the receiver fault, and the Coulomb stress was calculated at depths of 5 km and 10 km, respectively.

5. Discussion

5.1. Regional Coulomb Stress

After an earthquake, the stress distribution in the region will change [79]. The Comlomb3 software can draw a profile along a strike across a fault and calculate the Coulomb stress distribution on the profile after setting the fault dip. Additionally, the Coulomb3 software can overlay aftershock data on the layers and along the profile lines, and is able to show the depth and distribution characteristics of aftershocks in the subsurface on the profile. We selected the 2022 Menyuan earthquake seismogenic fault as the source fault and the Lenglongling fault as the receiver fault to calculate the Coulomb stress. We further analyzed the contribution of the 2022 Mengyuan earthquake to regional stress changes. From the planimetric distribution of aftershocks [37], the 2022 Menyuan mainshock was located on the south side of the intersection of the southwest wall of the Lenglongling fault and the south wall of the Tuolaishan fault (Figure 7). The aftershocks were mainly distributed in two directions. The aftershocks were distributed parallel to the Tuolaishan fault in the EW direction, and the Lenglongling fault in the NWW strike. Four section lines, AB, CD, EF, and GH, were placed along the faults in parallel and perpendicular directions to analyze the relationship between Coulomb stress and aftershocks (Figure 7c–f). Furthermore, the profiles showed that most aftershocks occurred at depths of 7–12 km.
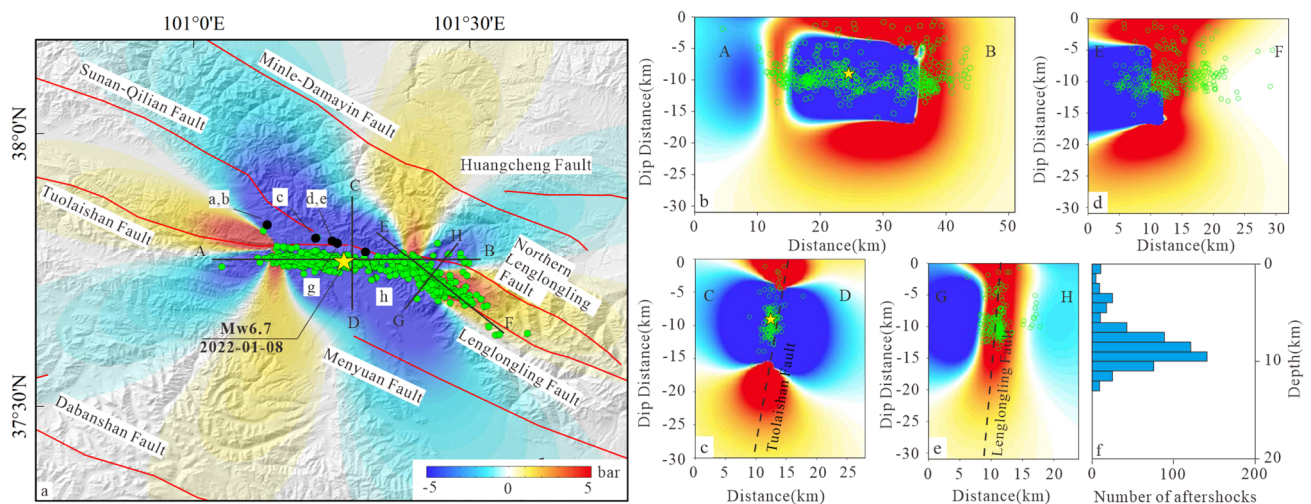

Figure 7. Aftershocks and Coulomb stress distribution of the 2022 event.

The AB section line was parallel to the Tuolaishan fault along the EW strike. Figure 7b reveals that the mainshock was located at the eastern Tuolaishan fault, and most aftershocks were in the Coulomb stress-release region. The CD section line was perpendicular to the Tuolaishan fault. Figure 7c shows that the mainshock and most aftershocks were located on the upper wall of the Tuolaishan fault. The majority of aftershocks were located in the Coulomb stress-release region. The EF and GH section lines were parallel and perpendicular to the Lenglongling fault. Figure 7e shows that aftershocks were distributed on both sides of the nearly perpendicular Lenglongling fault. The seismogenic fault was mainly concentrated in the Coulomb stress-release region. Aftershock distribution characteristics revealed that aftershocks distributed along the Tuolaishan fault were mainly concentrated on the southern wall of the fault. Coulomb stress was reduced in the aftershock distribution area. On the Lenglongling fault, aftershocks were concentrated on the fault's two sides. Coulomb stress increased in the aftershock distribution region. The 2022 Menyuan earthquake further enhanced the stress accumulation on the Lenglongling fault. The Coulomb failure stress change showed that the 2022 Menyuan earthquake generated considerable positive stress of more than 2 bar.

5.2. Seismic Hazard Due to Spatial Diversity of Surface Rupture of the 2022 Menyuan Earthquake

After the 2022 Menyuan earthquake, field observations demonstrated that the length of the surface rupture along the Lenglongling fault was ~26 km, along the Tuolaishan fault it was ~3.5 km, and the maximum left-lateral dislocation was located on the Lenglongling fault, at ~2.77 m [1]. Figure 7a shows five survey spots from a field investigation (points a-h) [1]. The field photographs of each observation point in Figure 8 demonstrate that the 2022 Menyuan earthquake formed a complex coseismic surface rupture zone constituting a combination of multiple types of ruptures, extrusion bulges, and scarps. The surface rupture was dominated by left-slip motion (Figure 8a), was mainly concentrated on the Lenglongling fault, and the rupture was characterized by left-rotation dislocations that exceed 2.2 m (Figure 8d,e). The 2022 Menyuan earthquake formed scarps approximately 95 cm high on the ice surface of the riverbed in localized areas (Figure 8f). The scarps indicated that the seismogenic fault had the characteristics of dip slip.
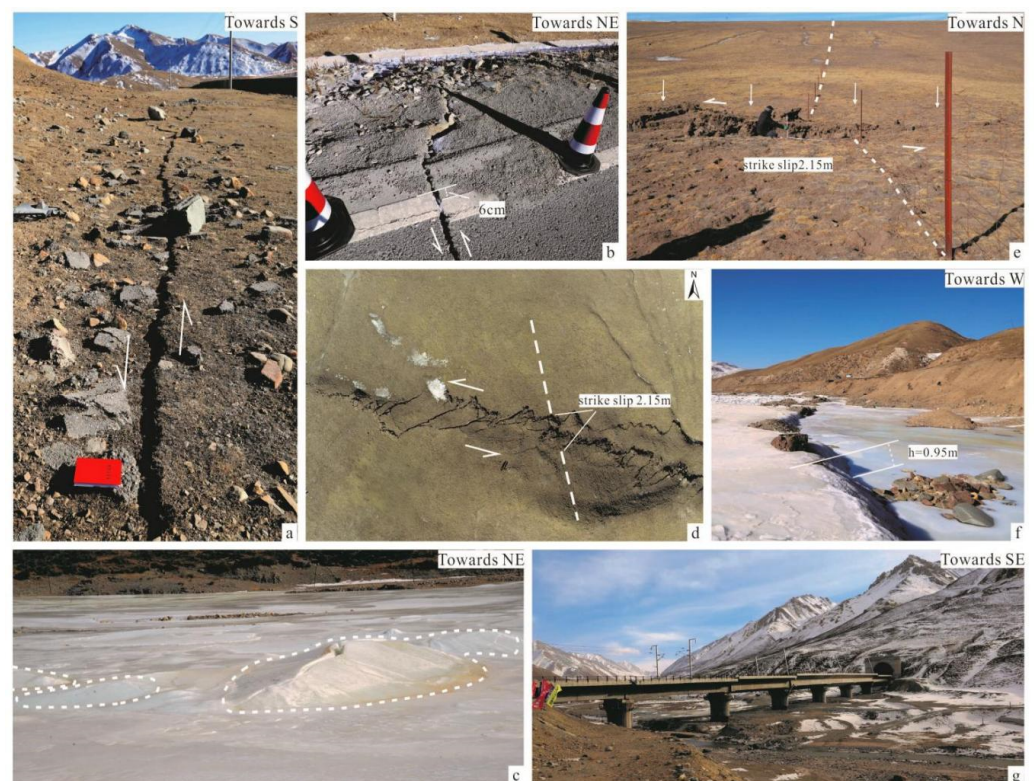

Figure 8. Field investigation results. (**a**) Ground fissure. (**b**) Highway left-slip dislocation. (**c**) Ice extrusion bulges. (**d**) Surface left-slip dislocation, associated with tension fissures. (**e**) Fence left-slip dislocation. (**f**) Scarps. (**g**) Railroad bridge overturned to the east.

The inversion shows that the maximum sliding depth of the 2022 Menyuan earthquake was ~4 km. The shallow fault rupture depth of this earthquake and the predominantly left-slip movement of the earthquake fault made it possible to form an apparent surface rupture at the ground surface. The 2022 Menyuan earthquake caused severe damage to local roads and bridges (Figure 8b,g). By comparing the GF-7 images, and coseismic deformation fields with the fault inversion model, Coulomb stress, and field survey results, we suggest that the seismogenic fault that caused the 2022 event was primarily a left slip with local reverse characteristics.

5.3. Seismogenic Structure

The Qilian orogenic belt is one of the most concentrated areas of strong tectonic deformation movements, including lateral escape from the northeastern Tibetan Plateau,

north–south crustal shortening, and rapid vertical uplift [80,81]. In this regional tectonic setting, the orogenic belt-scale flower structures formed by the Qilian-Haiyuan large strike-slip fault zone within Qilianshan modulate the region's differential motion [82]. Due to the variation in the orientation of different faults in the Haiyuan fault zone, two distinct extrusion-bending zones exist in the fault zone: the Haiyuan extrusion-bending zone and the Lenglongling extrusion-bending zone [83]. Extrusion-bending zones generally form reverse faults on both sides of the strike-slip faults with symmetrical and asymmetrical flower structures [24]. The north side of the Lenglongling fault has developed the Northern Lenglongling fault, the Minle-Damaying fault, and the Huangcheng-Shuangta fault, which reverses from south to north (Figure 9). The south side has developed the Menyuan fault, which reverses from north to south. These faults constitute the typical strike-slip asymmetric flower structure.
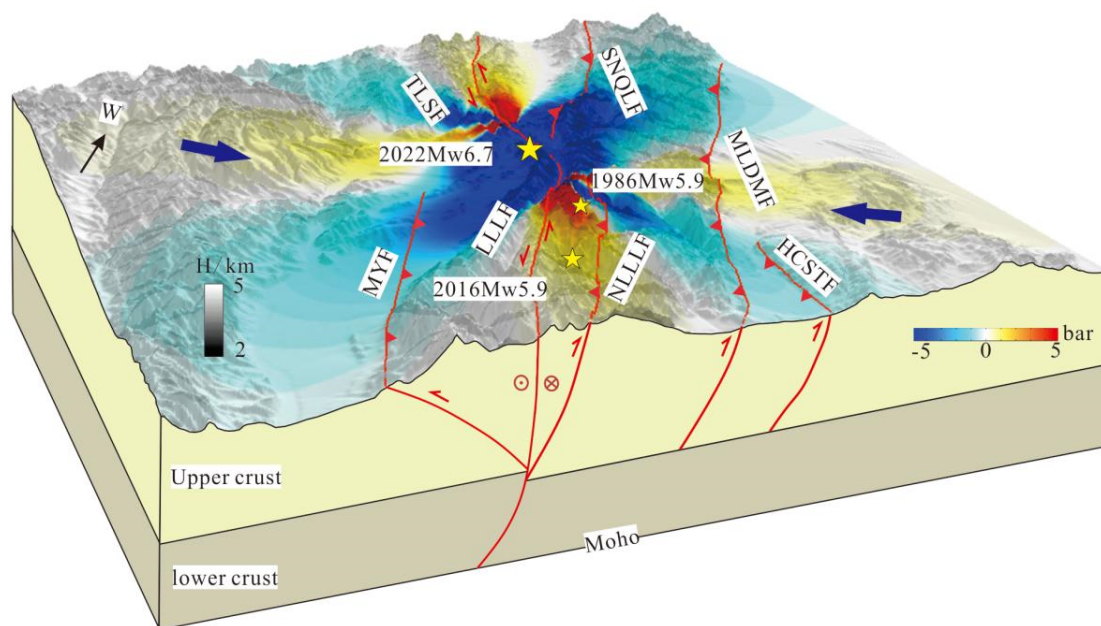
Figure 9. Flower structure of the Lenglongling fault. The fault location and regional crustal structure are from [82]. Blue arrow indicates the orientation of regional maximum principal compressive stress [84]. The regional Coulomb stress based on the 2022 Menyuan earthquake as the source fault and the Lenglongling fault as the receiver fault. MYF: Menyuan fault. TLSF: Tuolaishan fault. LLLF: Lenglongling fault. SNQLF: SuNan-Qilian fault. NLLLF: Northern Lenglongling fault. MLDMF: Minle-Damaying fault.

The GCMT results showed that the 1986 Mengyuan earthquake was a reverse-type earthquake. The inversion results and field investigations illustrated that the 2016 Menyuan earthquake was a reverse-type earthquake, and the 2022 Menyuan earthquake was a seismic event dominated by left-strike slip motion. The 1986 and 2016 earthquakes were on the Northern Lenglongling fault and caused further stress to increase on the Lenglongling fault. The Haiyuan fault is one of the main boundary faults in the northeastern Tibetan Plateau. The Lenglongling fault is an important component of the Haiyuan fault zone. Because of the long-term movement of the Indian plate in the NE direction of the Eurasian continent, rupture occurs when the stress accumulation exceeds the shear rupture strength of the Lenglongling fault's slip rupture. The Lenglongling fault triggered the rupture of the Tuolaishan fault at the same time, leading to the occurrence of the 2022 Menyuan earthquake. The three earthquakes also reflected the asymmetric fault structure of the Lenglongling fault.

6. Results

Through GF-7 image recognition, we recognized the ground-source earthquake rupture belt. Based on the Sentinel-1 SAR images, to obtain the coseismic deformation of the 2016 and 2022 earthquakes, we calculated the phase gradient and POT of the 2022 earthquake. Based on the coseismic deformation field of the 2016 and 2022 Menyuan earthquakes, the fault model and distributed slip model of the earthquake were inverted based on the elastic half-space rectangular dislocation theory. After comparing these with field investigation results, we calculated the Coulomb stress variations of the 1986, 2016, and 2022 events. We obtained the following conclusions:

(1) The maximum deformation in the LOS direction of the coseismic deformation field of the 2016 Menyuan earthquake was 8 cm. The maximum coseismic deformation field of the 2022 Menyuan earthquake in the LOS direction was 72 cm. The surface deformation of the 2022 Menyuan earthquake was determined to be concentrated on the Lenglongling fault by comparing the phase gradients and POT results. The surface rupture zone generally followed the WNW–ESE direction.

(2) The fault model of the InSAR coseismic deformation field inversion revealed that the maximum slip of the 2016 Menyuan earthquake was ~0.6 m, and the fault slip was mainly at depths of 4–10 km. The seismogenic fault of the 2016 event was the Northern Lenglongling fault. The maximum fault slip of the 2022 Menyuan earthquake was ~4 m, and fault slips were mainly at depths of 4–8 km. Based on how the GF-7 images were interpreted, the fault model, the distributed slip model, the Coulomb stress, the aftershocks, and field investigations, we considered the main seismogenic faults that broke during the 2022 event were the western Lenglongling fault and the Tuolaishan fault.

(3) The 2022 Menyuan earthquake Coulomb stress affected the Lenglongling fault, while the spatial diversity of the surface rupture zone indicated that the Lenglongling fault deformation and stress have continued to increase. The western segment of the Lenglongling fault is at risk of strong earthquakes in the future, and continuous observation of the fault activity is needed.

Conflicts of Interest: The authors declare no conflict of interest.

References

1. Liang, K.; He, Z.T.; Jiang, W.L.; Li, Y.S.; Liu, Z.M. Surface rupture characteristics of the Menyuan Ms6.9 Earthquake on January 8, 2022, Qinghai Province. *Seismol. Geol.* **2022**, *44*, 256–278. (In Chinese) [CrossRef]
2. Hu, C.Z.; Yang, P.X.; Li, Z.M.; Huang, S.T.; Zhao, Y.; Chen, D.; Xiong, R.W.; Chen, Q.Y. Seismogenic mechanism of the 21 January 2016 Menyuan, Qinghai Ms6.4 earthquake. *Chin. J. Geophys.* **2016**, *59*, 1637–1646. [CrossRef]
3. Xu, J.R.; Yao, L.X.; Wang, J. Earthquake source mechanisms of Menyuan earthquake (Ms = 6.4, on Aug.26,1986) and its strong aftershocks. *Chin. Earthq. Eng. J.* **1986**, *8*, 82–84. (In Chinese)
4. He, X.H.; Zhang, Y.P.; Shen, X.Z.; Zheng, W.J.; Zhang, D.L. Examination of the repeatability of two Ms6.4 Menyuan earthquakes in Qilian-Haiyuan fault zone (NE Tibetan Plateau) based on source parameters. *Phys. Earth Planet. Inter.* **2019**, *299*, 106–408. [CrossRef]
5. Jiang, W.L.; Li, Y.S.; Tian, Y.F.; Han, Z.J.; Zhang, J.F. Research of seismogenic structure of the Menyuan Ms6.4 earthquake on January 21, 2016 in Lenglongling area of NE Tibetan plateau. *Seismol. Geol.* **2017**, *39*, 536–549. (In Chinese) [CrossRef]
6. Gaudemer, Y.; Tapponnier, P.; Myer, B.; Peltzer, G.; Shunmin, G.; Zhitai, C. Partitioning of crustal slip between linked, active faults in the eastern Qilian Shan, and evidence for amajor seismic gap, the Tianzhu gap, on the western Haiyuan fault, Gansu (China). *Geophys. J. Int.* **1995**, *120*, 599–645. [CrossRef]
7. He, W.G.; Liu, B.C.; Yuan, D.Y.; Yang, M. Research on the slip rate of the Lenglongling fault zone. *Chin. Earthq. Eng. J.* **2000**, *22*, 90–97. (In Chinese)
8. Liu, F.B.; Wang, A.G.; Yuan, D.Y. Static Coulomb Stress changes and triggering interaction among strong earthquakes in the eastern segment of North Qilian Mountain. *Chin. Earthq. Eng. J.* **2014**, *36*, 360–371. (In Chinese)
9. Wu, D.L.; Qu, C.Y.; Zhao, D.Z.; Shan, X.J.; Han, C. Slip models of the 2016 and 2022 Menyuan, China, earthquakes, illustrating regional tectonic structures. *Remote Sens.* **2022**, *14*, 6317. [CrossRef]
10. Lindsey, E.O.; Natsuaki, R.; Xu, X.; Shimada, M.; Hashimoto, M.; Melgar, D.; Sandwell, D.T. Line-of-sight displacement from ALOS-2 interferometry: M-w 7.8 Gorkha earthquake and M-w 7.3 aftershock. *Geophys. Res. Lett.* **2015**, *42*, 6655–6661. [CrossRef]
11. Chen, K.J.; Avouac, J.P.; Aati, S.; Milliner, C.; Shi, C. Cascading and pulse-like ruptures during the 2019 Ridgecrest earthquakes in the Eastern California Shear Zone. *Nat. Commun.* **2020**, *11*, 22. [CrossRef]
12. Qu, W.; Liu, B.; Zhang, Q.; Gao, Y.; Chen, H.; Wang, Q.; Hao, M. Sentinel-1 InSAR observations of co-and post-seismic deformation mechanisms of the 2016 Mw 5.9 Menyuan Earthquake, Northwestern China. *Adv. Space Res.* **2021**, *68*, 1301–1317. [CrossRef]
13. Yang, H.F.; Wang, D.; Guo, R.; Xie, M.; Zang, Y.; Wang, Y.; Yao, Q.; Cheng, C.; An, Y.; Zhang, Y. Rapid report of the 8 January 2022 MS 6.9 Menyuan earthquake, Qinghai, China. *Earthq. Res. Adv.* **2022**, *2*, 100113. [CrossRef]
14. Luo, H.; Wang, T. Strain partitioning on the western Haiyuan fault system revealed by the adjacent 2016 Mw5. 9 and 2022 Mw6. 7 Menyuan earthquakes. *Geophys. Res. Lett.* **2022**, *49*, e2022GL099348. [CrossRef]
15. Okada, Y. Surface deformation due to shear and tensile faults in a Half Space. *Bull. Seismol. Soc. Am.* **1992**, *82*, 1018–1040. [CrossRef]
16. Tapponnier, P.; Xu, Z.Q.; Roger, F.; Meyer, B.; Arnaud, N.; Wittlinger, G.; Yang, J. Oblique stepwise rise and growth of the Tibet plate. *Science* **2001**, *294*, 1671–1677. [CrossRef]
17. Ding, L.; Kapp, P.; Wan, X.Q. Paleocene-Eocene record of ophiolite obduction and initial India-Asia collision, south central Tibet. *Tectonics* **2005**, *24*, TC3001. [CrossRef]
18. Wang, T.Y.; Li, G.B.; Elmes, M. Biostratigraphy and provenance analysis of the Cretaceous to Palaeogene deposits in southern Tibet: Implications for the India-Asia collision. *Basin. Res.* **2021**, *33*, 1749–1775. [CrossRef]
19. Xu, X.W.; Wu, X.Y.; Yu, G.H.; Tan, X.B.; Li, K. Seismo-geological signatures for identifying M ≥ 7.0 earthquake and their premilimary application in mainland China. *Seismol. Geol.* **2017**, *39*, 219–275. (In Chinese) [CrossRef]
20. Li, H.B.; Pan, J.W.; Sun, Z.M.; Si, J.L.; Pei, J.L.; Liu, D.L.; Marie, L.C.; Wang, H.; Lu, H.J.; Zheng, Y.; et al. Continental tectonic deformation and seismic activity: A case study from the Tibetan Plateau. *Acta Geol. Sin.* **2021**, *95*, 194–213. (In Chinese) [CrossRef]
21. Yuan, D.Y.; Zhang, P.Z.; Liu, B.C.; Gan, W.J.; Mao, F.Y.; Wang, Z.C.; Zheng, W.J.; Guo, H. Geometrical imagery and tectonic transformation of late Quaternary activate tectonics in northeastern margin of Qinghai-Xizang plateau. *Acta Geol. Sin.* **2004**, *78*, 270–278. (In Chinese)
22. Zheng, W.J.; Zhang, P.Z.; He, W.G.; Yuan, D.Y.; Shao, Y.X.; Zheng, D.W.; Ge, W.P.; Min, W. Transformation of displacement between strike-slip and crustal shortening in the northern margin of the Tibetan plateau: Evidence from decadal GPS measurements and late Quaternary slip rates on faults. *Tectonophysics* **2013**, *584*, 267–280. [CrossRef]
23. Jiang, W.L.; Jiao, Q.S.; Tian, T.; Zhang, J.F. Seismic slip distribution and rupture model of the Lenglongling Fault Zone, northeastern Tibetan Plateau. *Geol. J.* **2021**, *56*, 1299–1314. [CrossRef]
24. Pan, J.W.; Li, H.B.; Marie, L.C.; Liu, D.L.; Li, C.; Liu, F.C.; Wu, Q.; Lu, H.J.; Jiao, L.Q. Coseismic surface rupture and seismogenic structure of the 2022 Ms6.9 Menyuan earthquake, Qinghai Province, China. *Acta Geol. Sin.* **2022**, *96*, 215–231. (In Chinese) [CrossRef]
25. Lasserre, C.; Gaudemer, Y.; Tapponnier, P.; Meriaux, A.S.; Var der Woerd, J.; Yuan, D.Y.; Ryerson, F.J.; Finkel, R.C.; Caffee, M.W. Fast late Pleistocene slip rate on the Leng Long ling segment of the Haiyuan Fault, Qinghai, China. *J. Geophys. Res. Solid Earth* **2002**, *107*, 2276. [CrossRef]

26. Wu, D.L.; Ge, W.P.; Wei, C.M. Characteristics of present-day crustal defotmation along the Haiyuan fault zone using PS-InSAR method. *Chin. Earthq. Eng. J.* **2020**, *42*, 1055–1064. (In Chinese) [CrossRef]
27. Guo, P.; Han, Z.J.; An, Y.F.; Jiang, W.L.; Mao, Z.B.; Feng, W. Activity of the Lenglongling fault system and seismotectonics of the 2016 Ms6.4 Menyuan earthquake. *Sci. China Earth Sci.* **2017**, *60*, 929–942. (In Chinese) [CrossRef]
28. Huang, H.; Fu, H. A preliminary study of the seismogenic structure of the Now.23, 2015 Qilian 5.2 earthquake. *Earthquake* **2019**, *39*, 114–125. (In Chinese)
29. Li, Y.S.; Jiang, W.L.; Li, Y.J.; Shen, W.H.; He, Z.T.; Li, B.Q.; Li, Q.; Jiao, Q.S.; Tian, Y.F. Coseismic rupture model and tectonic implications of January 7 2022, Menyuan Mw6.6 earthquake constrains from InSAR observations and filed investigation. *Remote Sens.* **2022**, *14*, 2111. [CrossRef]
30. Li, Q.; Jiang, Z.S.; Wu, Y.Q.; Zhao, J.; Wei, W.X.; Liu, X.X. Present–day tectonic deformation characteristics of Haiyuan—Liuoanshan fault zone. *J. Geod. Geodyn.* **2013**, *33*, 18–22. [CrossRef]
31. Xu, G.Y.; Xu, X.W.; Yi, Y.N.; Wen, Y.M.; Wang, Q.X.; Li, K.; Ren, J.J. Seismogenic structure of the 2022 Menyuan Mw6.6 earthquake, Qinghai province, constrained by InSAR and Gaofen-7 observation. *Chin. J. Geophys.* **2022**, *65*, 4704–4724. [CrossRef]
32. Liu, J.; Klinger, Y.; Xu, X.W.; Lasserre, C.; Chen, G.H.; Chen, W.B.; Tapponnier, P.; Zhang, B. Millennial Recurrence of Large Earthquakes on the Haiyuan Fault near Songshan, Gansu Province, China. *Bull. Seismol. Soc. Am.* **2007**, *97*, 14–34. [CrossRef]
33. Guo, P.; Han, Z.J.; Mao, Z.B.; Xie, Z.D.; Dong, S.P.; Gao, F.; Gai, H.L. Paleoearthquakes and rupture behavior of the Lenglongling fault: Implications for seismic hazards of the northeastern margin of the Tibetan Plateau. *J. Geophys. Res. Solid Earth* **2019**, *124*, 1520–1543. [CrossRef]
34. Guo, P.; Han, Z.J.; Dong, S.P.; Yuan, R.M.; Xie, Z.D. Surface rupture and slip distribution along the Lenglongling fault in the NE Tibetan Plateau: Implications for faulting behavior. *J. Asian Earth Sci.* **2019**, *172*, 190–207. [CrossRef]
35. Guo, P.; Han, Z.J.; Gao, F.; Zhu, C.H.; Gai, H. A new tectonic model for the 1927 M8.0 Gulang earthquake on the NE Tibetan Plateau. *Tectonics* **2020**, *39*, e2020TC006064. [CrossRef]
36. Deng, Q.D.; Zhang, P.Z.; Ran, Y.K.; Yang, X.P.; Min, W.; Chun, Q.Z. Basic characteristics of active tectonics of China. *Sci. China Ser. D Earth Sci.* **2003**, *46*, 356–372. [CrossRef]
37. Fan, L.P.; Li, B.R.; Liao, S.R.; Jiang, C.; Fang, L.H. Precise relocation of the aftershock sequences of the 2022 M6.9 Menyuan earthquake. *Earthq. Sci.* **2022**, *35*, Q20220008. [CrossRef]
38. Poormirzaee, R.; Oskouei, M.M. Use of spectral analysis for detection of alterations in ETM data, Yazd, Iran. *Appl. Geomat.* **2010**, *2*, 147–154. [CrossRef]
39. Aati, S.; Milliner, C.; Avouac, J.-P. A new approach for 2-D and 3-D precise measurements of ground deformation from optimized registration and correlation of optical images and ICA-based filtering of image geometry artifacts. *Remote Sens. Environ.* **2022**, *277*, 113038. [CrossRef]
40. Lei, Y.; Gardner, A.; Agram, P. Autonomous Repeat Image Feature Tracking (autoRIFT) and Its Application for Tracking Ice Displacement. *Remote Sens.* **2021**, *13*, 749. [CrossRef]
41. Cao, H.Y.; Zhang, X.W.; Zhao, C.G.; Xu, C.; Mo, F.; Dai, J. 2020. System design and key tectnolongies of the GF-7 satellite. *Chin. Space Sci. Technol.* **2020**, *40*, 1–9. (In Chinese) [CrossRef]
42. Li, G.Y.; Tang, X.M.; Chen, J.Y.; Yao, J.Q.; Liu, Z.; Gao, X.M.; Zuo, Z.Q.; Zhou, X.Q. Processing and preliminary accuracy validation of the GF-7 satellite laser altimetry data. *Acta Geod. Cartograph. Sin.* **2021**, *50*, 1338–1348. (In Chinese) [CrossRef]
43. Jiao, Q.S.; Jiang, W.L.; Li, Q.; Lai, J.B.; Zheng, Y.; He, Z.T.; Shen, W.H.; Li, Y.S.; Luo, Y.; Zhang, J.F. Rapid emergency analysis of the surface related to the Qinghai Menyuan Ms6.9 earthquake on January 8, 2022, using GF-7 satellite images. *J. Remote Sens.* **2022**, *9*, 1895–1908. (In Chinese) [CrossRef]
44. Sandwell, D.T.; Mellors, R.; Tong, X.; Wei, M.; Wessel, P. Open radar interferometry software for mapping surface deformation. *Trans. Am. Geophys. Union* **2011**, *92*, 234. [CrossRef]
45. Xu, X.H.; Ward, L.; Jiang, J.L.; Smith–Konter, B.; Tymofyeyeva, E.; Lindsey, E.O.; Sylvester, A.G.; Sandwell, D. Surface creep rate of the southern San Andreas fault modulated by stress perturbations from nearby large events. *Geophys. Res. Lett.* **2018**, *45*, 10259–10268. [CrossRef]
46. Xu, X.H.; Sandwell, D.T.; Smith-Konter, B. Coseismic Displacements and Surface Fractures from Sentinel–1 InSAR: 2019 Ridgecrest Earthquakes. *Seismol. Res. Lett.* **2020**, *91*, 1979–1985. [CrossRef]
47. Chen, C.W.; Zebker, H.A. Phase unwarpping for large SAR interferograms: Statistical Segmentation and Generalized Network Models. *IEEE Trans. Geosci. Electron.* **2002**, *40*, 1709–1719. [CrossRef]
48. Chen, Y.; Penna, N.T.; Li, Z.H. Generation of real-time mode high-resolution water vapor fields from GPS observations. *J. Geophys. Res. Atmos.* **2017**, *122*, 2008–2025. [CrossRef]
49. Chen, Y.; Li, Z.H.; Penna, N.T.; Crippa, P. Generic atmospheric correction model for Interferometric Synthetic Aperture Radar observations. *J. Geophys. Res. Solid Earth* **2018**, *123*, 9202–9222. [CrossRef]
50. Chen, Y.; Li, Z.H.; Penna, N.T. Interferometric synthetic aperture radar atmospheric correction using a GPS–based iterative tropospheric decomposition model. *Remote Sens. Environ.* **2018**, *204*, 109–121. [CrossRef]
51. Rosen, P.A.; Gurrola, E.M.; Sacco, G.F.; Zebker, H. The InSAR scientific computing environment. In Proceedings of the EUSAR 2012, 9th European Conference on Synthetic Aperture Radar, Nuremberg, Germany, 23–26 April 2012.

52. Shan, X.J.; Qu, C.Y.; Gong, W.Y.; Zhang, Y.F.; Zhang, G.H.; Song, X.G.; Liu, Y.H.; Zhang, G.F. Coseismic deformation field of the Jiuzhaigou Ms7.0 earthquake from Sentinel–1A InSAR data and fault slip inversion. *Chin. J. Geophys.* **2017**, *60*, 4527–4536. (In Chinese) [CrossRef]
53. Sandwell, D.T.; Price, E.J. Phase gradient approach to stacking interferograms. *J. Geophys. Res. Solid Earth* **1998**, *103*, 1858–1862. [CrossRef]
54. Meade, C.; Sandwell, D.T. Synthetic aperture radar for geodesy. *Science* **1996**, *273*, 1181–1182. [CrossRef]
55. Elliott, J.R.; Walters, R.J.; Wright, T.J. The role of Space-Based observation in understanding and responding to active tectonics and earthquakes. *Nat. Commun.* **2016**, *7*, 13844. [CrossRef] [PubMed]
56. Poormirzaee, R.; Fister, I., Jr. Model-Based inversion of Rayleigh Wave Dispersion Curves via linear and nonlinear methods. *Pure Appl. Geophys.* **2021**, *178*, 341–358. [CrossRef]
57. Poormirzaee, R.; Kabgani, A. Characterizing the vs. profile from surface wave data using a customized artificial jellyfish search algorithm. *Pure Appl. Geophys.* **2022**, *179*, 4429–4444. [CrossRef]
58. Barnhart, W.D.; Lohman, R.B.; Mellors, R.J. Active accommodation of plate convergence in Southern Iran: Earthquake locations, triggered aseismic slip, and regional strain rates. *J. Geophys. Res. Solid Earth* **2013**, *118*, 5699–5711. [CrossRef]
59. Barnhart, W.D.; Murray, J.R.; Yun, S.-H.; Svarc, J.L.; Samsonov, S.V.; Fielding, E.J.; Brooks, B.A.; Milillo, P. Geodetic Constraints on the 2014 M 6.0 South Napa Earthquake. *Seismol. Res. Lett.* **2015**, *86*, 335–343. [CrossRef]
60. Barnhart, W.D. Fault creep rates of the Chaman fault (Afghanistan and Pakistan) inferred from InSAR. *J. Geophys. Res. Solid Earth* **2017**, *122*, 2016JB013656. [CrossRef]
61. Barnhart, W.D.; Hayes, G.P.; Wald, D.J. Global Earthquake Response with Imaging Geodesy: Recent Examples from the USGS NEIC. *Remote Sens.* **2019**, *11*, 1357. [CrossRef]
62. Sambridge, M. Geophysical inversion with a neighbourhood algorithm—I. Searching a parameter space. *Geophys. J. Int.* **1999**, *138*, 479–494. [CrossRef]
63. Lohman, R.B.; Simons, M. Some thoughts on the use of InSAR data to constrain models of surface deformation: Noise structure and data downsampling. *Geochem. Geophys. Geosyst* **2005**, *6*. [CrossRef]
64. Li, Y.S.; Jiang, W.L.; Zhang, J.F.; Luo, Y. Space Geodetic Observations and Modeling of 2016 Mw5.9 Menyuan Earthquake: Implications on Seismogenic Tectonic Motion. *Remote Sens.* **2016**, *8*, 519. [CrossRef]
65. Li, Z.H.; Han, B.Q.; Liu, Z.J.; Yu, C.; Chen, B.; Liu, H.H.; Du, J.; Zhang, S.C.; Zhu, W.; Zhang, Q.; et al. Source parameters and slip distributions of the 2016 and 2022 Menyuan, Qinghai earthquake constrained by InSAR observations. *Geomat. Inf. Sci. Wuhan Univ.* **2022**, *47*, 887–897. (In Chinese) [CrossRef]
66. Feng, W.P.; Li, Z.H.; Elliott, J.R.; Fukushima, Y.; Hoey, T.; Singleton, A.; Cook, R.; Xu, Z. The 2011Mw6.8 Burma earthquake: Fault constrains provided by multiple SAR techniques. *Geophys. J. Int.* **2013**, *195*, 650–660. [CrossRef]
67. Fukahata, Y.; Wright, T.J. A non–liner geodetic data inversion using ABIC for slip distribution on a fault with an unknown dip angle. *Geophys. J. Int.* **2008**, *173*, 353–364. [CrossRef]
68. Li, Y.S.; Feng, W.P.; Zhang, J.F.; Li, Z.H.; Tian, Y.F.; Jiang, W.L.; Luo, Y. Coseismic slip of the 2014 Mw6.1 Napa, California earthquake revealed by Sentinel–1A InSAR. *Chin. J. Geophys.* **2015**, *58*, 2339–2349. (In Chinese) [CrossRef]
69. Feng, W.P.; Samsonov, S.; Qiu, Q.; Wang, Y.Q.; Zhang, P.Z.; Li, T.; Zheng, W.J. Orthogonal fault rupture and rapid postseismic deformation following 2019 Ridgecrest, California, earthquake sequence revealed from geodetic observations. *Geophys. Res. Lett.* **2020**, *47*, E2019GL086888. [CrossRef]
70. Simons, M.; Fialko, Y.; Rivera, L. Coseismic deformation from the 1999 Mw7.1 Hector Mine, California, earthquake as inferred from InSAR and GPS observations. *Bull. Seismol. Soc. Am.* **2002**, *92*, 1390–1402. [CrossRef]
71. de Nardis, R.; Pandolfi, C.; Cattaneo, M.; Monachesi, G.; Cirillo, D.; Ferrarini, F.; Bello, S.; Brozzetti, F.; Lavecchia, G. Lithospheric double shear zone unveiled by microseismicity in a region of slow deformation. *Sci. Rep.* **2022**, *12*, 21066. [CrossRef]
72. Cirillo, D.; Totaro, C.; Lavecchia, G.; Orecchio, B.; Nardis, R.D.; Presti, D.; Ferrarini, F.; Bello, S.; Brozzetti, F. Structural complexities and tectonic barriers controlling recent seismic activity in the Pollino area (Calabria-Lucania, southern Italy)—Constraints from stress inversion and 3D fault model building. *Solid Earth* **2022**, *13*, 205–228. [CrossRef]
73. Galderisi, A.; Galli, P. Coulomb stress transfer between parallel faults. The case of Norcia and Mt Vettore normal faults (Italy, 2016 Mw 6.6 earthquake). *Results Geophys. Sci.* **2020**, *1–4*, 100003. [CrossRef]
74. Stein, R.S. The Role of stress transfer in earthquake occurrence. *Nature* **1999**, *402*, 605–609. [CrossRef]
75. Lin, J.; Stein, R.S. Stress triggering in reverse and subduction earthquakes, and stress interaction between the southern San Andreas and nearby reverse and strike–slip faults. *J. Geophys. Res. Solid Earth* **2004**, *109*, B02303. [CrossRef]
76. Toda, S.; Stein, R.S. Richards-Dinger, K.; Bozkurt, S.B. Forecasting the evolution of seismicity in southern California: Animations built on earthquake stress transfer. *J. Geophys. Res. Solid Earth* **2005**, *110*, B05S16. [CrossRef]
77. Toda, S.; Stein, R.S.; Sevilgen, V.; Lin, J. *Coulomb 3.3 Graphic-Rich Deformation and Stress-Change Software for Earthquake, Tectonic, and Volcano Research and Teaching—User Guide*; U.S. Geological Survey Open-File Report 2011—1060; USGS: Reston, VA, USA, 2011; 63p.
78. Wells, D.L.; Coppersmith, K.J. New empirical relationships among magnitude, rupture length, rupture width, rupture area, and surface displacement. *Bull. Seismol. Soc. Am.* **1994**, *84*, 974–1002. [CrossRef]
79. Harris, R.A. Introduction to special section: Stress triggers, stress shadows and implications for seismic hazard. *J. Geophys. Res. Solid Earth* **1998**, *103*, 24347–24358. [CrossRef]

80. Zheng, D.W.; Wang, W.T.; Wang, J.L.; Yuan, D.Y.; Liu, C.R.; Zheng, W.J.; Zhang, H.P.; Pang, J.Z. Progressive northward growth of the northern Qilianshan–Hexi Corridor (northeastern Tibet) during the Cenozoic. *Lithosphere* **2017**, *9*, 408–416. [CrossRef]
81. Zhang, P.Z.; Shen, Z.K.; Wang, M.; Gan, W.J.; Burgmann, R.; Wang, Q.; Niu, Z.J.; Sun, J.Z.; Wu, J.C.; Sun, H.R.; et al. Continuous deformation of the Tibetan Plateau from global positioning system data. *Geology* **2004**, *32*, 809–812. [CrossRef]
82. Feng, W.P.; He, X.H.; Zhang, Y.P.; Fang, L.H.; Sergey, S.; Zhang, P.Z. Seismic faults of the Mw6.6 Menyuan, Qinghai earthquake and their implication for the regional seismogenic structures. *Chin. Sci. Bull.* **2023**, *2-3*, 254–270. (In Chinese) [CrossRef]
83. Wang, H.; Liu, M.; Duan, B.; Cao, J.L. Rupture Propagation along Stepovers of Strike–Slip Faults: Effects of Initial Stress and Fault Geometry. *Bull. Seismol. Soc. Am.* **2020**, *110*, 1011–1024. [CrossRef]
84. Zhang, H.; Gao, Y.; Shi, Y.T.; Liu, X.F.; Wang, Y.X. Tectonic stress analysis based on the crustal seismic anisotropy in the northeastern margin of Tibetan Plateau. *Chin. J. Geophys.* **2012**, *55*, 95–104. [CrossRef]